Check for updates

Advanced Functional Materials

ADVANCED FUNCTIONAL MATERIALS
www.afm-journal.de

RESEARCH ARTICLE

Motion-Robust Multichannel sEMG Array for High-Fidelity Muscle Fatigue Monitoring

Yicong Wang[1] | Wenting Yu[2] | Senyun Yang[1] | Liang Zheng[1] | Hongnan Zhu[1] | Qiongyi Zhang[1] | Zhouyang Hu[1] | Jiangrui Gao[1] | Sanwei Hao[1] | Xianying Xu[2] | Ning Zhang[2] | Yuxing Bai[2] | Feng Xu[1] | Caofeng Pan[3] | Jun Yang[1]

[1]Beijing Key Laboratory of Lignocellulosic Chemistry, College of Materials Science and Technology, Beijing Forestry University, Beijing, People's Republic of China | [2]Department of Orthodontics, Beijing Stomatological Hospital and School of Stomatology, Capital Medical University, Beijing, People's Republic of China | [3]Beijing Key Laboratory for Atomic Manufacturing Equipment and Intelligent Sensing, Institute of Atomic Manufacturing, Beihang University, Beijing, People's Republic of China

Correspondence: Sanwei Hao (haosanwei@sdut.edu.cn) | Ning Zhang (dentistzhang112@ccmu.edu.cn) | Yuxing Bai (byuxing@ccmu.edu.cn) | Caofeng Pan (pancaofeng@buaa.edu.cn) | Jun Yang (yangjun11@bjfu.edu.cn)

Received: 20 August 2026 | **Revised:** 20 August 2026 | **Accepted:** 5 September 2026

Keywords: bacterial cellulose | eutectogel composite | flexible electrode array | high-fidelity sEMG | motion artifact suppression | muscle fatigue monitoring

ABSTRACT

Real-time muscle fatigue monitoring during dynamic activities is critical for preventing injury and optimizing performance, yet remains hindered by motion-induced signal artifacts in conventional wearable systems. Here, we present a motion-robust, multichannel surface electromyography (sEMG) array that enables high-fidelity neuromuscular signal acquisition and localized fatigue assessment during complex movements. The platform integrates a bacterial cellulose (BC)-reinforced heterogeneous eutectogel (BHE) with a hollow-patterned flexible printed circuit (FPC), wherein the BC network dissipates mechanical stress to preserve structural stability. This heterogeneous interface ensures seamless skin-electrode contact and suppresses signal distortion under motion. The six-channel FPC electrode configuration facilitates spatially resolved tracking of muscle synergy and fatigue progression. The system exhibits minimal resistance drift over 100 000 bending cycles and maintains impedance stability across a broad frequency range (1 to 10^5 Hz), achieving an average signal-to-noise ratio of 41 dB. In real-world scenarios, the device captures sEMG variations across localized muscle regions with reduced motion artifacts, enabling differential fatigue analysis. Furthermore, the model achieved 83.1% accuracy across four fatigue states in an independent external cohort comprising 160 samples from 40 previously unseen participants. This work demonstrates a wearable platform for continuous muscle monitoring with potential applications in sports science and rehabilitation.

1 | Introduction

Wearable bioelectronics are rapidly finding application in electrophysiological monitoring, enabling precise detection of bioelectric signals during daily activities, sports monitoring, and rehabilitation tasks, thereby providing physiological information for real-time health monitoring [1–3]. Within this landscape, accurate monitoring surface electromyography (sEMG) is particularly critical for evaluating muscle function and tracking fatigue [4]. Fatigue is a ubiquitous physiological state that alters muscle activation and force generation, thereby elevating the risk of musculoskeletal injury [5–7]. High-fidelity and

Yicong Wang, Wenting Yu and Senyun Yang contributed equally to this work.

All rights reserved, including rights for text and data mining and training of artificial intelligence technologies or similar technologies.
© 2026 Wiley-VCH GmbH

high-stability sEMG arrays show great potential in capturing multi-site muscular activity in real-life scenarios, enabling fine-grained motion decoding and detailed fatigue analysis [8]. Conventional sEMG arrays, however, are typically built on rigid electrodes and struggle to meet the stringent demands for flexible and biocompatible interface materials required for next-generation wearable electronics [9–11]. In contrast, sEMG arrays centered on adaptable on-skin electrodes have emerged as a compelling alternative to deliver low-motion artifact in data quality across a wide range of applications [12, 13]. Their superior mechanical compliance, deformability, and biocompatibility allow them to accommodate skin mechanics and provide non-invasive interfaces for acquiring sEMG signals. These systems enable decoding of muscle activation patterns, tracking of fatigue progression, and interpretation of movement intention [8, 14–17]. Despite these advantages, acquiring high-fidelity sEMG signals under dynamic and vigorous motion remains challenging. During vigorous motion, when the skin undergoes complex deformation, mechanical mismatch between the electrode and skin can cause high interfacial impedance and motion artifacts [18, 19]. These persistent issues underscore the need for next-generation multichannel sEMG arrays with flexible electrodes capable of sustaining high mechanical compliance, low impedance, and robust signal fidelity under real-world usage.

In recent years, flexible electrode materials such as gallium-based liquid metals [20–22], carbon nanomaterials [23], and intrinsically conductive polymers [24, 25] have been integrated into sEMG arrays to ensure the mechanical compliance necessary for stable signal acquisition under dynamic motion. For example, Yang et al. [26] developed a stretchable bioelectrode array using a microscale confined adhesion strategy to pattern liquid metal circuits with fine resolution (150 μm) and ultrahigh stretchability (up to 600% strain). The device demonstrated excellent durability over 20 000 cycles and, when integrated with a deep learning model, it achieved 93% accuracy in real-time gesture recognition, offering a reliable solution for wearable electrophysiological monitoring and human-machine interaction. A parallel line of research by Hassan et al. [27] reported an organic, flexible neural interface for non-penetrating, single-neuron recording from the human cortical surface. The device used PEDOT:PSS electrodes on a perforated substrate to achieve stable, high-quality neural signals, successfully isolating 229 single units with clear pyramidal and interneuron discrimination, and thus provided a clinically viable tool for high-resolution human brain mapping. Although these attempts provide excellent compliance, they still undergo mechanical deficiency and interfacial instability under the large, repeated, and frequent bending deformation of natural skin physical motion, leading to elevated impedance, motion-induced artifacts, and inferior signal fidelity in sEMG arrays [28, 29]. To better accommodate skin deformation, soft-electrode arrays often incorporate geometry-based designs such as serpentine interconnects [30–33] and island–bridge layouts [3, 34, 35], which redistribute strain and reduce local stress to improve device-level deformability under large strain without signal recording fluctuation. However, these strategies remain insufficient for regions with pronounced curvature or large local bending, underscoring the need for an integrated material–structure approach [36–38].

Herein, we report a hollow patterned sEMG array (HP-BHEA), featuring mechanical compliance, biocompatibility, and high signal fidelity that integrates a bacterial cellulose (BC) film-reinforced heterogeneous eutectogel electrode (BHE) with a laser-cut hollow patterned flexible printed circuit (FPC) substrate for reliable sEMG acquisition under dynamic motion. Within the eutectogel, hydrogen-bonding interactions between the amide groups of polyacrylamide (PAM) and the hydroxyl groups on BC microfibers enhance its structural stability, allowing consistent electrode performance under repeated bending and deformation. These mechanical and electrical stabilities allow the eutectogel to function as a reliable electrode material within the HP-BHEA, ensuring high-fidelity signal acquisition even under dynamic motion. To monitor muscle-group fatigue precisely, a six-channel electrode configuration is deliberately incorporated into the HP-BHEA to capture distributed muscle activations, enabling region-specific decoding of neuromuscular dynamics and revealing distinct fatigue behaviors in agonistic and antagonistic muscle groups during complex movements. These features collectively allow HP-BHEA to acquire high-fidelity sEMG signals under dynamic motion, enable precise multichannel fatigue assessment, and offer potential applications in sports science, rehabilitation, and human–machine interfaces.

2 | Results

2.1 | Conceptual Overview of the Multichannel sEMG Patch

Real-time muscle fatigue monitoring in dynamic exercise is essential for optimizing athletic performance and preventing exercise-induced injuries. However, achieving reliable and multichannel sEMG monitoring under realistic training conditions remains challenging. Conventional rigid electrodes suffer from poor mechanical compliance and discomfort, while most hydrogel-based electrodes are prone to dehydration and susceptible to premature mechanical failure during monitoring [39]. Consequently, high-fidelity signal acquisition under prolonged and vigorous motion has not yet been reliably realized. To address these persistent limitations, we develop a multichannel surface electromyography platform that combines an adaptable on-skin eutectogel electrode and a laser-cut hollow patterned FPC substrate. This platform exhibits high mechanical compliance with the skin, maintains stable sEMG signal acquisition under dynamic motion, and enables muscle fatigue assessment during realistic training scenarios.

As shown in Figure 1a, the system employs a flexible electrode array positioned on the upper arm, enabling stable skin–electrode interfacing during motion and simultaneous monitoring of electrophysiological signals from both the biceps and triceps. The electrodes are spatially distributed to capture localized, muscle-specific activation patterns during strength training. The acquired multichannel sEMG signals are continuously transmitted to an external processing module, where they are visualized, analyzed, and used to extract fatigue-related features for each channel.

To ensure stable signal acquisition under the large and repetitive deformations encountered during dynamic exercise, the electrode array integrates eutectogel electrodes with a laser-cut,

16163028, 0, Downloaded from https://advanced.onlinelibrary.wiley.com/doi/10.1002/adfm.78406 by Beihang University (Buaa), Wiley Online Library on [23/09/2026]. See the Terms and Conditions (https://onlinelibrary.wiley.com/terms-and-conditions) on Wiley Online Library for rules of use; OA articles are governed by the applicable Creative Commons License

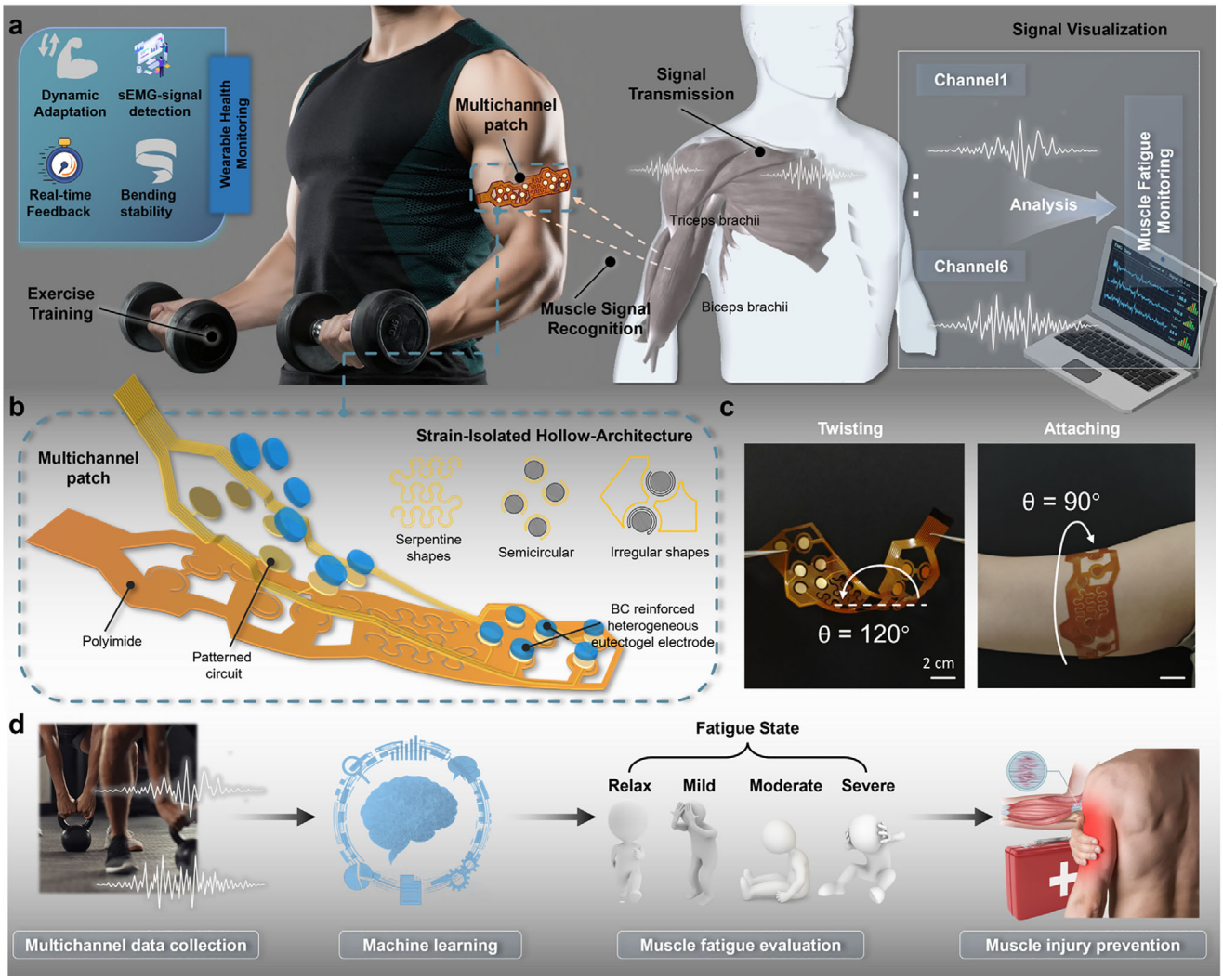


FIGURE 1 | System-level design and working principle of the multichannel sEMG patch for real-time muscle fatigue monitoring. (a) Conceptual illustration of the multichannel surface electromyography (sEMG) patch laminated on the upper arm, conformally interfacing with skin to simultaneously record localized electrical activity from the biceps and triceps during dynamic strength training. Multichannel sEMG signals are transmitted to an external module for real-time visualization, feature extraction, and fatigue evaluation. (b) Strain-isolated, open-architecture device layout based on a laser-cut patterned flexible printed circuit (FPC) substrate. Serpentine, semicircular, and irregular interconnect geometries are employed to redistribute and relax mechanical strain, while the bacterial cellulose–reinforced heterogeneous eutectogel ensures stable conductive pathways under deformation. (c) Photographs demonstrating the mechanical robustness of the device under large twisting ($\theta = 120°$) and its intimate conformal attachment on curved biological surfaces ($\theta = 90°$). Scale bar: 2 cm. (d) Schematic workflow of the multichannel sEMG–based fatigue assessment and protection system. High-fidelity multichannel signals are processed using a deep learning model to classify muscle fatigue states (relaxed, mild, moderate, and severe), enabling real-time fatigue evaluation and guidance for muscle injury prevention.

hollow-patterned flexible printed circuit (FPC) substrate (Figure 1b). The array adopts a six-channel configuration comprising twelve electrode sites, designed to adequately cover the key muscle groups of the upper arm, particularly the biceps and triceps brachii, enabling spatially resolved monitoring of sEMG during dynamic exercises. For on-body operation, the electrode array is affixed to the arm skin using medical-grade adhesive tape, while the flexible FPC substrate ensures conformal skin contact and wearability during movement. From a structural perspective, the FPC serves as a mechanically compliant substrate and provides reliable multichannel signal acquisition. Conformability to the curved upper arm is enhanced by selectively removing non-functional substrate regions, which largely reduces the bending stiffness of the device. In addition, serpentine, semicircular, and irregular interconnect geometries are used to redistribute applied strain and suppress stress concentration in the metal traces. As a result, local deformation of the conductive pathways remains minimal even when the entire device undergoes large twisting ($\theta = 120°$) or conforms to curved surfaces such as the upper arm ($\theta = 90°$), as illustrated in Figure 1c. This integrated, strain-isolated open architecture helps reduce the risk of cracking or plastic deformation of the conductive pathways and limits relative motion at the electrode–skin interface, which supports stable multichannel sEMG signal acquisition during dynamic movement.

A critical component of this array is a eutectogel electrode that is engineered to combine mechanical compliance and

16163028, 0, Downloaded from https://advanced.onlinelibrary.wiley.com/doi/10.1002/adfm.78406 by Beihang University (Buaa), Wiley Online Library on [23/09/2026]. See the Terms and Conditions (https://onlinelibrary.wiley.com/terms-and-conditions) on Wiley Online Library for rules of use; OA articles are governed by the applicable Creative Commons License

biocompatibility, enabling stable and high-fidelity bioelectric signal acquisition during motion. The eutectogel electrode is composed of a polyacrylamide (PAAm) network, a choline chloride-glycerol-based deep eutectic solvent (DES), PEDOT:PSS, and a bacterial cellulose (BC) film (Figures S4 and S5). Upon free-radical polymerization, acrylamide monomers crosslink into a three-dimensional PAAm network, forming a mechanically robust yet compliant gel matrix, while the choline chloride–glycerol DES remains as a non-volatile solvent phase that supports stable ionic transport during prolonged operation. Within this eutectogel, PEDOT:PSS is incorporated to provide electronically conductive pathways, with the PSS component functioning as a dopant and dispersant that stabilizes the PEDOT chains and promotes their uniform dispersion. When added to the acrylamide–DES precursor, PEDOT:PSS assembles into a percolated conductive network within the PAAm matrix, driven by electrostatic interactions and hydrogen bonding between the sulfonate groups of PSS and the amide groups of PAAm [40, 41]. Mechanical robustness under large deformation is achieved through the incorporation of the BC film as a reinforcing framework, which serves as the primary stress-bearing component to facilitate efficient stress transfer and strain-energy dissipation through hydrogen bonding with the surrounding eutectogel matrix.

The multichannel sEMG data acquired by this sEMG patch are further processed using a time-distributed CNN–BiLSTM model to identify muscle fatigue states (Figure 1d). The sEMG patch acquires multichannel sEMG signals from the upper arm during dynamic exercise, and the raw signals are subsequently preprocessed through filtering and segmentation to suppress motion artefacts and to generate fixed-length input windows. These windowed multichannel segments are then fed into the CNN–BiLSTM model, in which the CNN layers extract spatiotemporal representations from each channel while the BiLSTM captures temporal dependencies across consecutive segments. The trained network outputs the predicted fatigue level for each time window based on the recorded sEMG data, enabling subsequent analysis of muscle fatigue states throughout the exercise task. Overall, integrating soft multichannel sEMG sensing with deep-learning-based analysis provides an approach for neuromuscular fatigue assessment under dynamic conditions.

2.2 | Characterization of BHE

The BC reinforced heterogeneous eutectogel (BHE) is architected as a heterogeneous composite, integrating a rigid BC framework with a soft PAAm polymer matrix. Microscopically, the BC provides a continuous, interpenetrating nanofibrous skeleton that confers mechanical strength and dimensional stability (Figure 2a). Unlike dispersed cellulose fillers, the continuous BC scaffold provides extended stress-transfer pathways throughout the composite (Note S3 and Table S4). This fibrous network is infiltrated by the highly flexible PAAm eutectogel, which, being rich in hydrogen-bonding sites, establishes intimate contact with the BC framework via extensive robust intermolecular interactions [42]. On a macroscopic scale, this synergy gives rise to a tightly interlocked "hard–soft" structure, stabilized by hydrogen bonds and chain entanglements between the BC hydroxyls and PAAm amide groups. Within this architecture, the cellulose fibers serve as the primary stress-bearing component, while the PAAm phase provides elasticity, thereby enabling efficient stress transfer and imparting remarkable structural robustness under deformation.

Within this heterogeneous architecture, the overall mechanical response can be effectively tailored by adjusting the polymer composition. To clarify the role of PAM content, the tensile behaviors of heterogeneous eutectogels with different PAM concentrations (20, 30, and 40 wt.%) were compared (Figure S6). The eutectogel containing 30 wt.% PAM exhibits the champion tensile strength (~570 kPa) while maintaining good deformability. By contrast, the 20 wt.% PAM sample shows lower tensile strength but higher elongation at break, whereas further increasing the PAM content to 40 wt.% leads to reduced extensibility and earlier failure. These observations indicate that an intermediate PAM content provides a favorable balance between network connectivity and polymer chain mobility, which is critical for achieving optimal mechanical performance. In addition, peel tests show a relatively high peeling force between PAM and BC, and microscopy images reveal residual PAM on the BC surface after peeling, indicating cohesive failure within PAM (Figure S7). These results confirm strong PAM–BC interfacial interactions, which contribute to the enhanced mechanical performance of BHE.

The presence of such intermolecular interactions is supported by Fourier transform infrared (FTIR) spectroscopy (Figure S8). Compared with the PAM-based homogeneous eutectogel without BC (PHE), the BHE exhibits a markedly broadened O—H stretching band at 3200–3600 cm^{-1}, indicating enhanced hydrogen-bonding interactions. A subtle broadening of the amide I band (~1650 cm^{-1}) is also observed, suggesting hydrogen bonding between the carbonyl groups of PAAm and the hydroxyl groups of BC. In addition, a characteristic cellulose absorption band at ~1160 cm^{-1} is observed, confirming the successful incorporation of BC into the eutectogel network. Beyond molecular-scale interactions, the mesoscale structural integrity and compositional homogeneity of the BHE were examined by scanning electron microscopy (SEM) and energy-dispersive x-ray spectroscopy (EDS). Surface SEM images reveal a continuous and compact morphology without apparent phase separation, while the corresponding EDS elemental mapping demonstrates uniform spatial distributions of C, N, O, and Cl throughout the eutectogel matrix (Figure S9). This homogeneous integration of the BC scaffold with the PAAm matrix establishes a continuous interphase, providing a structural basis for efficient stress transfer and reliable mechanical performance.

Having established the structural advantages of the BHE, we further evaluate whether this heterogeneous architecture concept is applicable across different polymer matrices. To this end, we implement the same design across various polymer systems including poly (N, N-dimethylacrylamide) (PDMAA), poly (2-(N-3-Sulfopropyl-N, N-dimethylammonium)ethyl methacrylate) (PSBMA), polyacrylic acid (PAA), poly-methacryloyloxyethyltrimethylammonium chloride (PDMC), poly-2-Hydroxyethyl-Acrylate (PHEA), and polydiacetone acrylamide (PDAAM), respectively (Figure 2b). Remarkably, despite their chemical diversity, all viable composites exhibit consistent enhancements in both Young's modulus and toughness relative to their homogeneous counterparts

16163028, 0, Downloaded from https://advanced.onlinelibrary.wiley.com/doi/10.1002/adfm.78406 by Beihang University (Buaa), Wiley Online Library on [23/09/2026]. See the Terms and Conditions (https://onlinelibrary.wiley.com/terms-and-conditions) on Wiley Online Library for rules of use; OA articles are governed by the applicable Creative Commons License

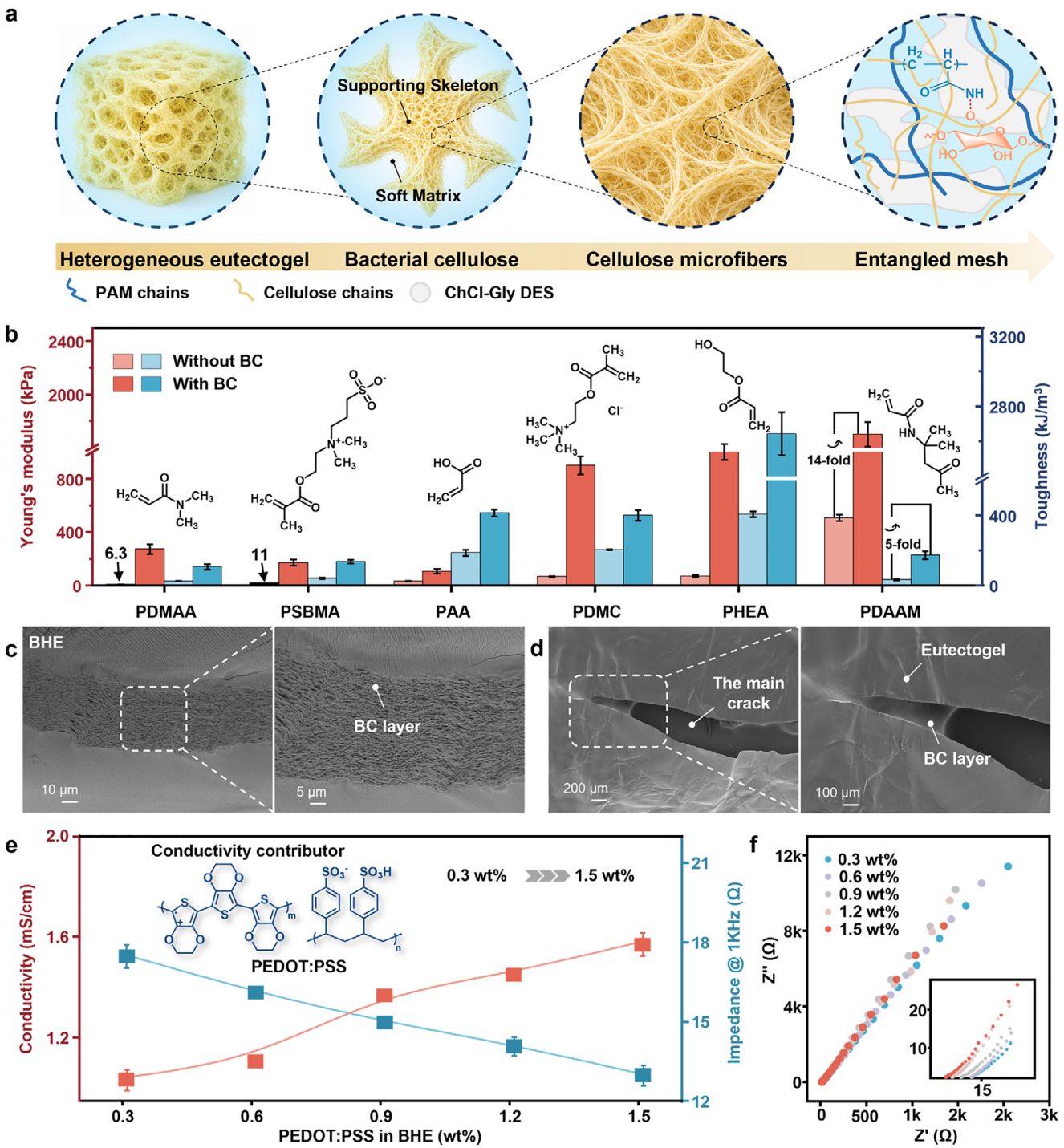


FIGURE 2 | Structural configuration, mechanical enhancement, and electrical performance of the bacterial cellulose–reinforced heterogeneous eutectogel (BHE). (a) Schematic of the BHE architecture, comprising a bacterial cellulose (BC) fibrous scaffold embedded within a soft eutectogel matrix to form a hierarchically heterogeneous network. (b) Generalizability of the BHE strategy across various polymer matrices (PDMAA, PSBMA, PAA, PDMC, PHEA, and PDAAM), demonstrating significant improvements in Young's modulus and fracture toughness. Error bars represent the standard deviation (n = 3 independent samples). (c) Cross-sectional scanning electron microscopy (SEM) images of the BHE. The left panel shows the overall layered structure, while the right panel reveals the dense, continuous BC fibrous network. (d) SEM images of the crack morphology in the BHE. The left panel highlights the macroscopic crack path, and the right panel shows the crack tip region, illustrating crack blunting and high fracture resistance. (e) Electrical conductivity of the BHE as a function of PEDOT:PSS concentration. (f) Corresponding Nyquist plots, indicating impedance behavior modulated by conductive polymer content.

16163028, 0, Downloaded from https://advanced.onlinelibrary.wiley.com/doi/10.1002/adfm.78406 by Beihang University (Buaa), Wiley Online Library on [23/09/2026]. See the Terms and Conditions (https://onlinelibrary.wiley.com/terms-and-conditions) on Wiley Online Library for rules of use; OA articles are governed by the applicable Creative Commons License

(Figure S10). For instance, the PDAAM-based heterogeneous eutectogel demonstrates over a 14-fold increase in modulus and a 5-fold improvement in toughness, highlighting the exceptional energy dissipation and crack resistance endowed by the heterogeneous architecture.

To quantitatively assess the extent of the mechanical enhancements in BHE, we further examine these mechanical enhancements through tearing and pre-notched shear tests. The force–displacement curves reveal that the BHE sustains a peak load nearly double that of the PHE, approximately 4 N versus 2 N, alongside greater fracture displacement, 180 mm compared to 150 mm, indicating improved strength and deformability (Figure S11a). Moreover, the pre-cracked BHE retains high fracture energy, suggesting enhanced resistance to crack propagation. In sharp contrast, this reinforcement was absent in the PHE, which exhibits early failure and low fracture energy (Figure S11b,c). Quantitatively, the BHE achieves a tear strength above 400 N m^{-1} and a fracture energy exceeding 700 kJ m^{-2}, outperforming the PHE by 10 times (Figure S11d). These findings collectively highlight the mechanical robustness imparted by the heterogeneous architecture, thus providing a solid platform for maintaining structural integrity and signal stability of sEMG electrode arrays during dynamic muscle fatigue monitoring.

Beyond resistance to fracture, the ability to withstand dynamic deformation is equally critical for practical applications. We further evaluated the dynamic viscoelastic behavior of BHE and PHE by rheological characterization (Figure S12). Frequency sweep measurements show that the BHE exhibits higher storage (G′) and loss (G″) moduli across the 0.1–100 Hz range than PHE, indicating a more robust and interconnected network. Consistently, BHE retained 79% of its initial stress after 1800 s at a fixed strain of 20%, compared with 31% for PHE (Figure S13), supporting its improved time-dependent mechanical stability.

In practical use as electrodes for epidermal electromyography arrays, the BHE is continuously subjected to repeated bending and tensile cycling caused by skin stretching during muscle activation. Therefore, resistance to crack initiation and propagation is essential for preserving the structural and functional integrity. Cross-sectional scanning electron microscopy (SEM) imaging (Figure 2c) confirms a dense and continuous BC nanofibrous network embedded within the soft matrix, which acts as an internal reinforcing barrier. As shown in Figure 2d, an advancing crack becomes blunted and deflected upon encountering the BC layer, rather than propagating freely through the material. This crack deflection behavior explains the improved fracture resistance of BHE under repeated deformation.

Building upon this mechanically reinforced framework, we next introduce PEDOT to regulate electrical transport. The BHE exhibits stable electrical resistance over time across a broad PEDOT loadings of 0.3–1.5 wt.% (Table S1). As depicted in Figure 2e, the electronic conductivity increases monotonically with PEDOT content, reaching approximately 1.9 mS·cm^{-1} at 1.5 wt.%. Consistently, the impedance at 1 kHz decreases with increasing PEDOT loading (Figure S14). Beyond 1.5 wt.%, however, PEDOT aggregation compromises structural homogeneity, establishing this concentration as the optimal trade-off between conductivity and dispersion. Electrochemical impedance spectroscopy (EIS) further confirms reduced interfacial and bulk resistance at higher PEDOT contents (Figure 2f). While the electrical transport is primarily governed by the PEDOT network, the BC scaffold contributes to maintaining conductive-network integrity under deformation. During continuous abrasion, BHE maintained electrical continuity for approximately 800 s, compared with approximately 200 s for PHE (Figure S15), indicating improved electrical stability under repeated surface wear. These results support the use of BHE as a mechanically robust and electrically stable electrode material.

2.3 | Bending Resistance and Biocompatibility Assessment

The structural integrity of electrode materials under repeated bending deformation is critical for maintaining stable electrical signal acquisition in flexible electronics. To evaluate the long-term electromechanical durability of the electrodes, cyclic bending tests were conducted for up to 100 000 cycles under continuous 90° bending, which approximates the curvature encountered in typical human joint motions during daily activity wearable applications (Movie S1). Owing to its BC-reinforced heterogeneous architecture, the 100 000-cycle-reliable bending BHE exhibits exceptional electromechanical stability under repeated bending, as evidenced by a comparative analysis of resistance evolution during cyclic bending, which reveals distinct electrical degradation behaviors among different electrode structures. As shown in Figure 3a, the PHE exhibits pronounced cumulative electrical signal degradation, with resistance variation reaching up to 104% after 100 000 bending cycles. In contrast, the BHE maintains minimal resistance fluctuation (11.9%) throughout the entire test, indicating improved electrical stability under continuous 90° bending. This stability is further corroborated by current–time responses and discrete current distribution analysis, in which the BHE demonstrates a higher mean current amplitude and a narrower distribution compared to the broadly dispersed current profile observed for the PHE (Figure 3b; Figure S16). In addition, the mechanical robustness of the BHE is also preserved after cyclic bending. Tearing tests performed after the 100 000-cycle bending show that the BHE retains tearing resistance comparable to its pristine state, with only moderate reductions in tearing strength (Figure S17). Collectively, these electrical and mechanical robustness results demonstrate that the three-dimensional fibrous network of the heterogeneous architecture effectively dissipates bending-induced stress while preserving structural integrity under continuous bending.

Complementing these findings on long-term cycling stability, we further investigate the electromechanical performance of the electrodes under complex mechanical deformation conditions, including multi-angle bending and folding along different directions. For the bending tests, both BHE and PHE are subjected to sequential deformation using a horizontal tensile testing machine, undergoing bending from a flat state (0°) to 60°, 120°, 180°, and then returning to the initial flat state (Figure 3c; Figures S19 and S20). The real-time resistance–time profiles demonstrate that the BHE maintains stable electrical performance with minimal resistance variation throughout the entire bending sequence, exhibiting nearly constant values with limited fluctuation. In contrast, the PHE shows increased resistance and

16163028, 0, Downloaded from https://advanced.onlinelibrary.wiley.com/doi/10.1002/adfm.78406 by Beihang University (Buaa), Wiley Online Library on [23/09/2026]. See the Terms and Conditions (https://onlinelibrary.wiley.com/terms-and-conditions) on Wiley Online Library for rules of use; OA articles are governed by the applicable Creative Commons License

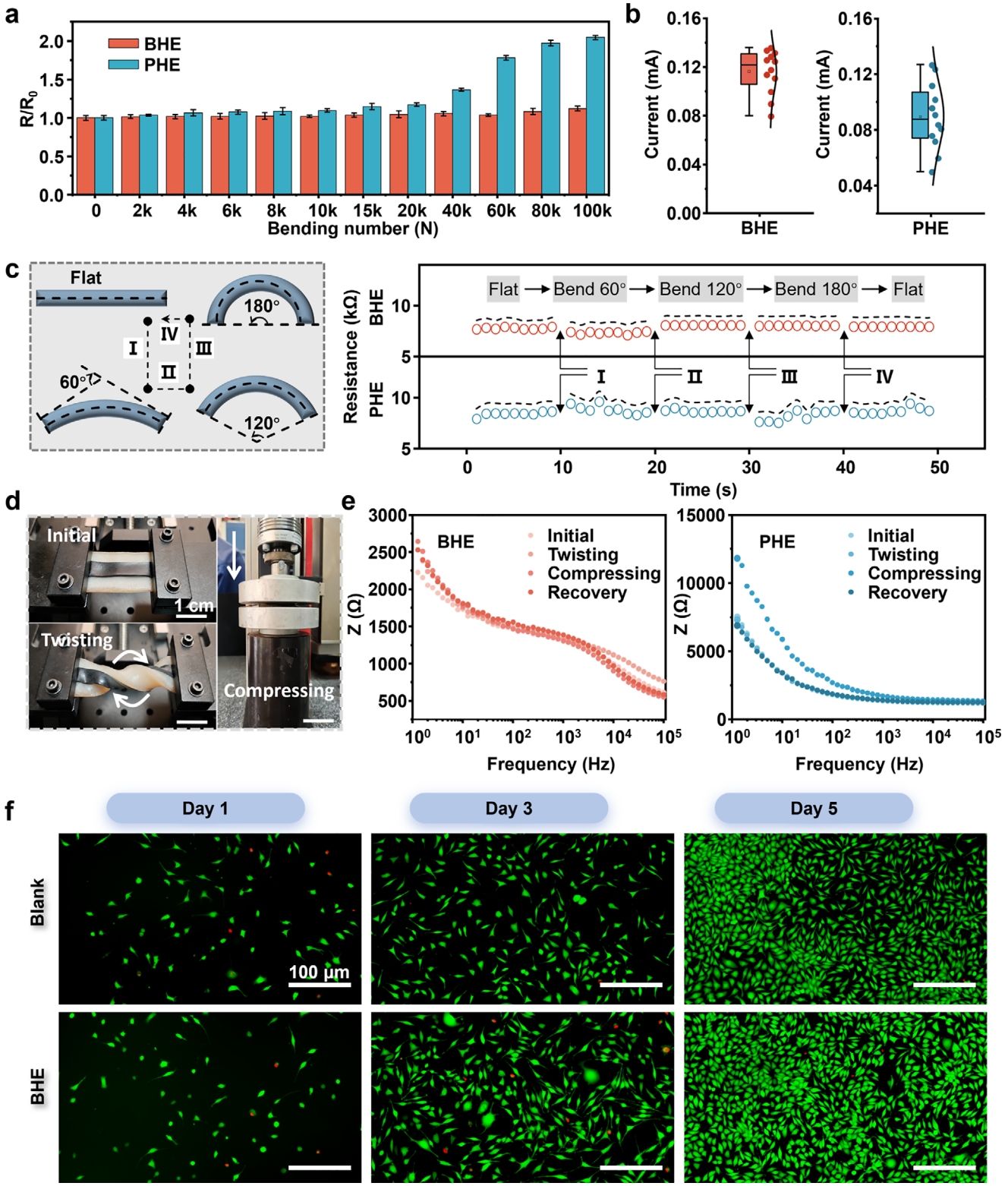


FIGURE 3 | Electromechanical durability and biocompatibility evaluation of the BHE. (a) Cyclic bending stability of the BHE and pristine eutectogel (PHE) electrodes under continuous 90° bending for 100 000 cycles. Resistance variation is expressed as R/R_0, where R_0 is the initial resistance. (b) Discrete distribution of current signal intensity recorded throughout the bending cycles, indicating the signal consistency of BHE over time. (c) Resistance evolution of BHE and PHE electrodes under cyclic bending at different angles (0°, 60°, 120° and 180°, respectively), showing angle-independent mechanical compliance and electrical stability. (d) Photographs of the mechanically controlled twisting and compression tests of the BHE. Scale bar: 1 cm. (e) Bode plots of impedance magnitude for BHE and PHE electrodes adhered to human skin under various motion conditions, highlighting impedance stability of the BHE. (f) Live/dead staining images of cells cultured for 1, 3, and 5 days, comparing the BHE treatment group with blank controls. Scale bar: 100 μm. Three independent replicates yielded similar results.

16163028, 0, Downloaded from https://advanced.onlinelibrary.wiley.com/doi/10.1002/adfm.78406 by Beihang University (Buaa), Wiley Online Library on [23/09/2026]. See the Terms and Conditions (https://onlinelibrary.wiley.com/terms-and-conditions) on Wiley Online Library for rules of use; OA articles are governed by the applicable Creative Commons License

signal deviation, particularly at larger bending angles. Beyond bending-angle dependence, the electromechanical robustness is further evaluated under sequential folding along different directions. The relative resistance change (R/R_0) of both electrodes is measured during folding and subsequent recovery. As shown in Figure S21a, the BHE electrode exhibits negligible resistance variation throughout the folding–recovery process, with R/R_0 remaining close to unity, indicating stable electrical performance under direction-dependent deformation. By comparison, the PHE (Figure S21b) displays an increased resistance and incomplete recovery after folding along different directions, suggesting irreversible disruption of conductive pathways within the homogeneous gel matrix. Overall, these results highlight the critical role of structural heterogeneity and fibrous reinforcement in preserving continuous and reliable charge transport under diverse mechanical deformation modes, independent of bending angle or folding direction.

Evaluation of the electrode–skin interface impedance for the BHE and PHE electrodes is further conducted under repetitive mechanical deformation to examine their electrical stability and mechanical robustness. Both electrodes are attached to human skin and subjected to cyclic twisting and compression (200 cycles each) to simulate dynamic operational conditions, with the corresponding impedance spectra (Z–f) recorded at four distinct stages: initial, twisting, compression, and after both deformations. Figure 3d presents a representative photograph of the BHE during testing. For the BHE (Figure 3e, left), the impedance magnitude exhibits minimal variation across the entire frequency range (1–10^5 Hz), maintaining consistent impedance characteristics after repeated deformation. The slight decrease in low-frequency impedance likely results from improved interfacial wetting due to perspiration of the skin, whereas the high-frequency region remains nearly unchanged, indicating preservation of the intrinsic bulk conductivity. This stability underscores the excellent mechanical compliance and structural integrity of the heterogeneous architecture, which sustains deformation while maintaining continuous ionic and electronic conduction pathways. To further evaluate measurement reproducibility, the deformation-dependent impedance measurements were repeated using three independently prepared samples from different batches under the same twisting and compression conditions, showing consistent trends in both impedance magnitude (Figure S22). In summary, these findings substantiate that the BHE achieves superior electrical stability and mechanical resilience under cyclic mechanical loading, emphasizing the critical role of structural heterogeneity and fibrous reinforcement in maintaining consistent signal transmission for flexible bioelectronic applications.

The cytocompatibility of the BHE electrode is evaluated using mouse fibroblast cells (L929 cells). As shown in Figure 3f, cells in the BHE group display well-spread morphologies and show increasing proliferation from day 1 to day 5. LIVE/DEAD fluorescence imaging shows predominantly viable cells with minimal dead-cell signals, comparable to the blank control throughout the culture period. Consistently, quantitative analysis (Figure S23) indicates that cell viability with the BHE treatment remains close to 100% after 3 days of incubation. These results suggest that the BHE forms a biointerface with low cellular perturbation, fulfilling a key requirement for bioelectronic devices intended for prolonged contact with living tissues.

2.4 | Electrophysiological Signal Capturing Performance

The mechanical integrity of sEMG electrodes under dynamic deformation is critical for reliable electrophysiological monitoring. As schematically illustrated in Figure 4a, the BHE employs a BC film as a structural framework, whose three-dimensional fibrous network dissipates mechanical stress. When subjected to periodic bending from dynamically curved skin surfaces, this hierarchical architecture enables efficient dissipation of normal and shear stresses through the BC fiber matrix, thereby preventing localized stress concentration. In contrast, Ag/AgCl electrodes with limited bendability are prone to structural instability under similar deformation.

To evaluate the influence of mechanical robustness on sEMG signal acquisition, we compare Ag/AgCl electrodes against the bend-tolerant BHE with heterogeneous structure through 200 repetitive bending cycles during sEMG recording on upper arm muscles. Owing to its mechanically stabilized heterogeneous architecture, the BHE effectively resists motion-induced disturbance, enabling reliable sEMG signal acquisition throughout continuous muscle activity (Figure 4b). In contrast, Ag/AgCl electrodes with limited bendability are mechanically vulnerable to stress concentration under cyclic bending. The BHE demonstrates SNR and RMS values as high as 42.04 ± 5.41 dB and 173.23 ± 24.25 μV before bending, respectively (Figure 4c,d). Following 200 bending cycles, BHE retained higher SNR and RMS values than Ag/AgCl electrodes (36.84 ± 5.87 vs 30.04 ± 5.80 dB and 158.76 ± 16.92 vs 109.78 ± 6.57 μV, respectively; $p < 0.001$; $n = 20$ paired measurements). These results indicate that BHE better preserves sEMG signal quality under repeated bending. Consistent with these dynamic bending results, Figure S24 further confirms that the BHE with heterogeneous structure enables high-fidelity sEMG signal acquisition under tensile and compressive deformations, indicating robust signal stability across diverse mechanical loading modes.

Muscle fatigue resulting from training serves as a direct precursor to sport-related injuries and chronic pain, thus underscoring the necessity for accurate assessment of muscle fatigue state during training. To evaluate the muscle fatigue state, sEMG signals (Figure S25) from human subjects during rest and isometric contraction are analyzed. The temporal variations in frequency-domain features, including the median frequency (MDF) and mean frequency (MNF), are shown in Figure 4e,f. As muscle contraction continues, both features gradually decrease, indicating fatigue progression. When the subject can no longer sustain the load, the load is released, and the duration before this point is defined as the endurance time. After unloading, both features rapidly return to their baseline values (approximately 50 Hz). As shown in Figure 4g, a linear relationship is observed between these two frequency-domain features and time during isometric contraction, with negative slopes of 0.05 for MDF and 0.02 for MNF, confirming fatigue development. The linear decay of these spectral parameters provides a quantitative framework for objectively tracking fatigue progression.

16163028, 0, Downloaded from https://advanced.onlinelibrary.wiley.com/doi/10.1002/adfm.78406 by Beihang University (Buaa), Wiley Online Library on [23/09/2026]. See the Terms and Conditions (https://onlinelibrary.wiley.com/terms-and-conditions) on Wiley Online Library for rules of use; OA articles are governed by the applicable Creative Commons License

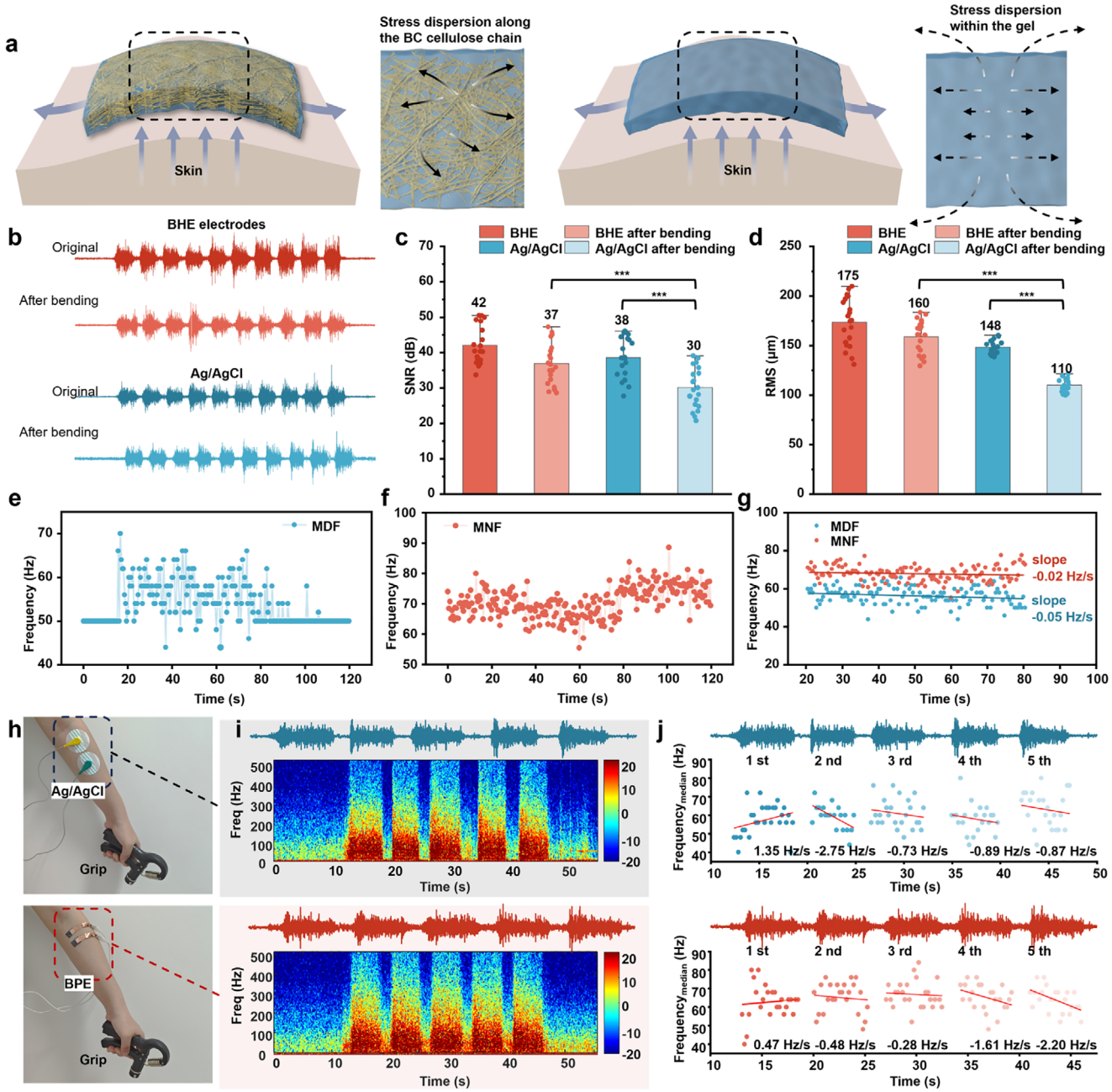


FIGURE 4 | Electrophysiological signal acquisition performance of the BHE compared with commercial Ag/AgCl electrodes under dynamic conditions. (a), Schematic comparison of mechanical stress dissipation during skin bending between the bend-tolerant BHE and conventional Ag/AgCl electrodes. (b) Representative sEMG signals acquired by BHE and Ag/AgCl electrodes during dynamic wrist flexion tasks, shown before and after repeated bending. (c) Signal-to-noise ratio (SNR) and (d) root mean square (RMS) values of sEMG signals recorded using BHE and commercial Ag/AgCl electrodes before and after 200 bending cycles. Data are presented as mean ± SD with individual data points shown (n = 20 paired measurements). Statistical significance was analyzed using paired statistical comparisons. ***$p < 0.001$. (e) Temporal evolution of median frequency (MDF) and (f) mean frequency (MNF) during an isometric contraction task, demonstrating fatigue-related spectral shifts. (g) Linear regression of MDF and MNF over time, highlighting frequency decay trends associated with muscle fatigue progression. (h) Photographic setup showing electrode placement on the flexor carpi ulnaris muscle. Two electrode pairs (BHE and Ag/AgCl) are symmetrically attached to the same forearm region. (i) Time-frequency spectrograms of sEMG signals recorded by Ag/AgCl electrodes and BHE during wrist curls with a 5 kg dumbbell over five repetitions. (j) Median frequency trends extracted from the sEMG signals of each flexion cycle (first to fifth repetition), showing consistent fatigue-induced decline for both electrode types. BHE demonstrates comparable or improved tracking fidelity relative to Ag/AgCl electrodes.

16163028, 0, Downloaded from https://advanced.onlinelibrary.wiley.com/doi/10.1002/adfm.78406 by Beihang University (Buaa), Wiley Online Library on [23/09/2026]. See the Terms and Conditions (https://onlinelibrary.wiley.com/terms-and-conditions) on Wiley Online Library for rules of use; OA articles are governed by the applicable Creative Commons License

In addition to fatigue assessment, sEMG analysis is also widely used in clinical diagnosis to evaluate muscle health through frequency-domain parameters. Typically, a gradual decrease in MNF and MDF indicates muscle fatigue, while an immediate decrease at the beginning of contraction suggests pathological changes because only a limited number of muscle fibers can be recruited for activation. To verify the capability of the BHE in capturing frequency information (MNF), BHE and Ag/AgCl electrodes are placed at the same position on the muscle belly of the flexor carpi ulnaris (Figure 4h). Figure 4i displays the corresponding spectrograms of the arm sEMG signal obtained during five wrist flexion tasks after short-time Fourier transform processing, showing the energy distribution of the recorded signals. Notably, the BHE demonstrates superior signal stability with reduced background noise at both 100 and 300 Hz, whereas Ag/AgCl electrodes exhibit substantial interference at these frequencies. These tasks are designated as flexion 1 to 5, with the corresponding MDF calculated for each movement cycle (Figure 4j). Both BHE and Ag/AgCl electrodes exhibit a transition from an initial positive or near-neutral MDF slope to negative slopes across repeated contractions, indicating the onset of muscle fatigue under dynamic conditions. These findings confirm that the BHE improves signal stability during dynamic sEMG monitoring while maintaining comparable fatigue-assessment capability.

Furthermore, it is well established that time-domain features of sEMG signals, reflecting signal magnitude, exhibit linear correlations with muscle strength. Intermittent grip strength tests were conducted on the right hand across varying force levels. Figure S26 presents the acquired sEMG signals and corresponding time-domain features extracted during these intermittent contractions. The results reveal a distinct positive correlation between applied force level, sEMG signal amplitude, and the magnitude of all analyzed time-domain parameters, confirming these features as reliable indicators for muscle force estimation under dynamic testing conditions. BHE was then used to quantify fatigue progression under different mechanical loads (Figure S27a). As shown in Figure S27b, increasing the isometric contraction load from 49 to 98 N and further to 147 N leads to a progressive decrease in the frequency value recorded at the upper limit of endurance (F-point), from 152 Hz to 135 Hz and 113 Hz, respectively. Concurrently, endurance time decreases from 330 s to 77 s and 54 s, respectively. This inverse relationship between applied load and endurance parameters aligns with fundamental exercise physiology principles, where higher loading accelerates fatigue development.

2.5 | HP-BHEA for Muscle Location and Fatigue Assessment

sEMG monitoring during dynamic physical activities faces challenges in maintaining signal fidelity due to motion-induced artifacts and intermittent skin-electrode contact. To address these limitations, we have developed an integrated sEMG recording system designed for stable operation under dynamic conditions (Figure 5a). The system architecture comprises three key elements: a conformable multi-channel electrode array for stable signal acquisition (HP-BHEA), a front-end signal conditioning circuit for analog-to-digital conversion and signal preprocessing, and a back-end connector for data transmission (Figure S28). Within this architecture, physiological signals captured by the electrode array are processed through the onboard circuitry and subsequently transmitted to external devices for visualization and analysis (Figures S29 and S30). This integrated approach addresses the need for reliable sEMG monitoring during dynamic motion.

The HP-BHEA incorporates a laser-cut hollow patterned FPC layer as both the encapsulation and substrate, together with a patterned copper circuit layer defining six signal acquisition channels (Figure 5b). This hollow patterned architecture enables stress redistribution through semicircular apertures around the electrodes, serpentine interconnects within the array, and irregular micro-perforations between electrode sites, thereby reducing local stress concentration, improving bending compliance, and minimizing slippage during deformation (Figure S31). This patterned FPC substrate provides essential mechanical support while the copper traces ensure reliable electrical connectivity across all six channels. Together, this integrated design maintains mechanical support, electrical connectivity, and stable skin contact during bending-dominated dynamic movements.

To evaluate signal stability under dynamic bending conditions, we developed two types of electrode arrays: one array integrated with BHE (HP-BHEA) and another incorporating commercial Ag/AgCl electrodes. Both arrays maintained identical structural parameters and channel configurations, and contained six channels for simultaneous sEMG recording during dynamic curl testing. Time–frequency spectrograms of the recorded sEMG signals reveal consistent periodic high-energy bands in both electrode arrays during dynamic muscle contractions, confirming effective signal acquisition across all channels (Figure 5c). Notably, the spectrograms obtained from HP-BHEA exhibit sharper temporal boundaries and reduced background noise. In contrast, the Ag/AgCl electrode array shows broader spectral distributions accompanied by elevated baseline noise and occasional spectral leakage into adjacent frequency bands. Consistently, during the contraction phase, only two channels of the Ag/AgCl array maintain SNR values above 10 dB, while all six channels of the BHE array consistently exceed this critical threshold (Figure S32). These results indicate that the BHE-based array better maintains signal integrity under mechanically demanding conditions.

After verifying the signal stability and reliability of the HP-BHEA, it was further employed for muscle activity monitoring during dumbbell biceps curls, selected as a representative strength-training task, as they are widely used to develop the biceps and triceps brachii muscles. Since improper loading strategies or excessive training intensity may increase the risk of musculoskeletal injury, continuous monitoring of muscle activation and fatigue during such movements is important for injury prevention and training optimization (Figure S33). During combined isometric and dynamic tasks with different loads, sEMG signals were simultaneously recorded from the biceps and triceps brachii using the HP-BHEA (Figure S34; Figure 5d,e). Channels 1–3 positioned over the biceps brachii exhibit higher RMS values than channels 4–6 located on the triceps brachii, reflecting the dominant involvement of the biceps brachii as the agonist muscle during elbow flexion (Figure 5f; Figure S35). The RMS amplitudes also increase progressively with

16163028, 0, Downloaded from https://advanced.onlinelibrary.wiley.com/doi/10.1002/adfm.78406 by Beihang University (Buaa), Wiley Online Library on [23/09/2026]. See the Terms and Conditions (https://onlinelibrary.wiley.com/terms-and-conditions) on Wiley Online Library for rules of use; OA articles are governed by the applicable Creative Commons License

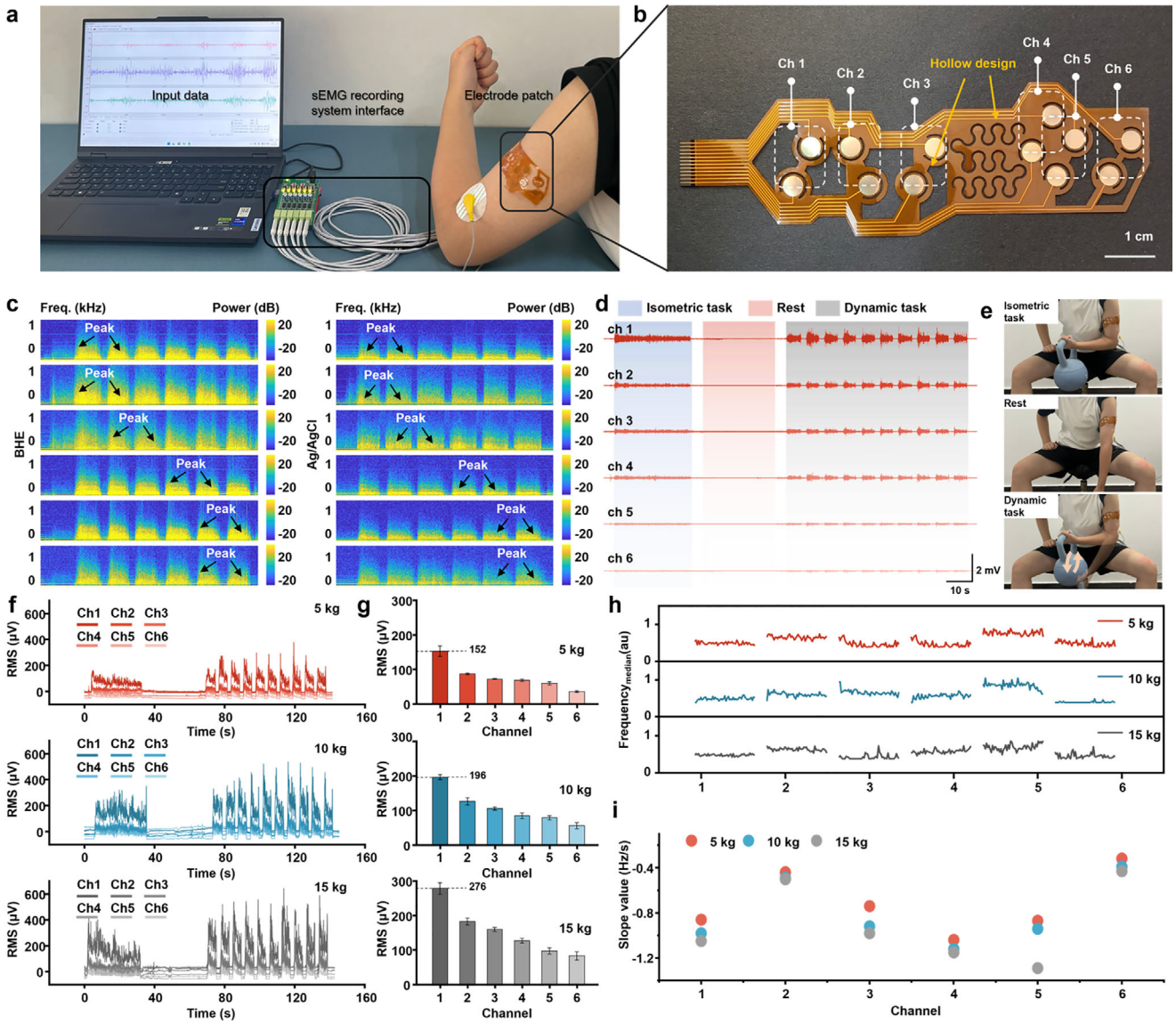


FIGURE 5 | System-level performance evaluation of the HP-BHEA for dynamic multichannel sEMG monitoring. (a) Schematic of the full system setup incorporating the hollow-patterned BHE array (HP-BHEA) for dynamic sEMG recording. A custom-designed back-end connector enables independent access to all six electrode channels. (b) Structural layout of the HP-BHEA prior to eutectogel electrode integration. White-dotted regions represent circuit modules, each with six channels interconnected via copper traces. Half-circular, serpentine, and irregular etching patterns on the flexible printed circuit (FPC) enhance mechanical compliance (yellow arrows). (c) Time–frequency spectrograms of sEMG signals recorded from the biceps and triceps brachii during dynamic curl exercises using HP-BHEA (left array with BHE electrodes) and commercial Ag/AgCl electrodes (right array). (d) Representative sEMG waveforms from all six channels of the HP-BHEA during wrist curl with a 5 kg load, capturing activation patterns from both muscle groups. (e) Photographs documenting the experimental procedure involving isometric holding, resting, and dynamic movement phases. (f) Amplitude envelopes of sEMG signals acquired from each channel under varying loads, illustrating load-dependent signal modulation. (g) Root mean square (RMS) values of sEMG signals during dynamic tasks across all six channels under different loading conditions. (h) Mean frequency values of the sEMG signals during dynamic tasks, demonstrating consistent spectral behavior across channels and loadings. (i) Slope of linear fits to median frequency values during isometric contraction, recorded from all six channels under varying loads, reflecting load-dependent fatigue progression.

external loads ranging from 5 to 15 kg during both isometric and dynamic contractions (Figure 5g). At 10 and 15 kg, the RMS values show pronounced elevations during the final repetitions, indicating fatigue accumulation during exercise. Spectral analysis further shows consistent median frequency declines across all channels with increasing loads (Figure 5h). Linear fitting of frequency trends yields negative slope values whose magnitudes increase with loading intensity (Figure 5i). These RMS and spectral results together demonstrate the feasibility of using HP-BHEA for neuromuscular monitoring under the tested training conditions.

2.6 | Deep Learning-Assisted Muscle Fatigue State Recognition

Typical manually extracted features of sEMG signals, such as frequency-domain indices and their temporal slopes, can partially

16163028, 0, Downloaded from https://advanced.onlinelibrary.wiley.com/doi/10.1002/adfm.78406 by Beihang University (Buaa), Wiley Online Library on [23/09/2026]. See the Terms and Conditions (https://onlinelibrary.wiley.com/terms-and-conditions) on Wiley Online Library for rules of use; OA articles are governed by the applicable Creative Commons License

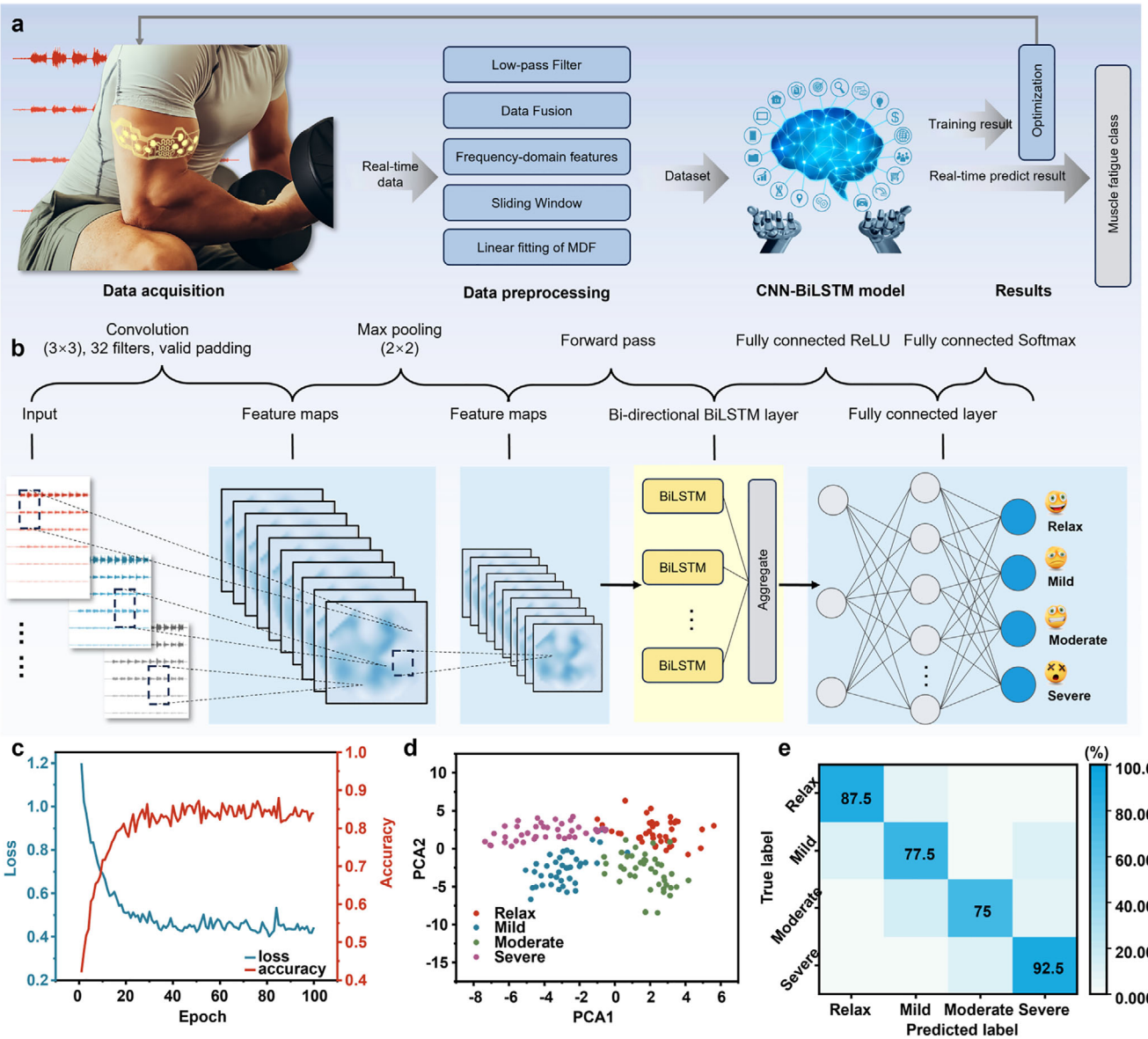


FIGURE 6 | Deep learning-enabled classification of muscle fatigue states based on multichannel sEMG signals. (a) Schematic workflow of the real-time muscle fatigue classification module. The pipeline includes a model training stage using labeled sEMG data and a practical deployment stage for real-time fatigue state recognition. (b) Architecture of the proposed deep learning model combining a convolutional neural network (CNN) and bidirectional long short-term memory (BiLSTM) layers for spatiotemporal feature extraction from sEMG signals. (c) Training performance curves of the CNN–BiLSTM model, showing loss and classification accuracy over epochs for both training and test datasets. (d) t-distributed stochastic neighbor embedding (t-SNE) visualization of sEMG features corresponding to four distinct muscle fatigue states. Each point represents a signal sample projected from high-dimensional feature space to two-dimensional space. (e) Confusion matrix of the CNN–BiLSTM model, demonstrating accurate classification performance across four fatigue levels (relaxed, mild, moderate, and severe).

reflect the state of muscle fatigue. However, given the complexity, variability, and individual differences in muscle fatigue, such conventional features are limited in their ability to comprehensively characterize its underlying patterns, particularly the coupled spatial and temporal variations in multichannel recordings. To address these limitations, machine learning is introduced as a complementary analytical tool to extract data-driven representations from high-dimensional multichannel sEMG signals and support fatigue-state discrimination during exercise.

As illustrated in Figure 6a, the model-development workflow consists of four main components: data preprocessing, dataset construction, model training, and optimization. Specifically, the data preprocessing module comprises a sequence of substeps that transform raw multichannel sEMG recordings into image-based representations, thereby facilitating subsequent dataset formulation in the form of input–label pairs (X, Y) and enabling efficient model training [43]. The processed dataset is then utilized to train a supervised deep learning model. Subsequently, an optimization strategy is implemented to identify and exclude EMG channels that exhibit limited or adverse contributions to fatigue classification accuracy, with the aim of enhancing both model performance and computational efficiency.

16163028, 0, Downloaded from https://advanced.onlinelibrary.wiley.com/doi/10.1002/adfm.78406 by Beihang University (Buaa), Wiley Online Library on [23/09/2026]. See the Terms and Conditions (https://onlinelibrary.wiley.com/terms-and-conditions) on Wiley Online Library for rules of use; OA articles are governed by the applicable Creative Commons License

Here we use a deep network named the CNN-BiLSTM model (Figure 6b), which is applied for the classification of sEMG signals recorded during exercise. Convolutional neural networks (CNNs) are first employed to hierarchically extract representative local features from the multichannel sEMG inputs, leveraging convolutional kernels to capture spatial patterns with high translational invariance. Nevertheless, CNN architectures are limited in modeling temporal dependencies in time-series signals. To address this limitation, the CNN layers are embedded within a time-distributed framework, enabling the network to preserve temporal structure while extracting spatial features at each time step. This design allows the model to jointly characterize spatial correlations across channels and temporal variations within the signal sequence. Furthermore, a bidirectional long short-term memory (BiLSTM) network is integrated to capture long-range temporal dependencies by processing feature sequences in both forward and backward directions. Through this combination, the CNN-BiLSTM architecture enables joint modeling of spatial and temporal features for sEMG-based muscle fatigue classification. In this framework, the MDF/MNF-based analysis and the CNN–BiLSTM serve complementary functions. Direct MDF/MNF analysis provides interpretable channel-level indicators of fatigue-related spectral changes, whereas the CNN–BiLSTM enables integrated and automated processing of continuous multichannel sEMG sequences.

Based on this framework, four fatigue states are defined based on the number of fatigued channels among the six-channel HP-BHEA recordings: 0 fatigued channels indicates no fatigue; 1–2 indicates mild fatigue; 3–4 indicates moderate fatigue; and 5–6 indicates severe fatigue (Figure S36). Each state was recorded 200 times, resulting in a dataset of 800 collected sEMG signals. All 800 samples collected from the original cohort of 100 participants were used to train the final deep-learning model. A separate independent cohort comprising 160 labeled sEMG samples from 40 newly recruited participants was reserved exclusively for external evaluation. These 40 participants were entirely distinct from those included in the original training cohort. The external cohort was not incorporated into model fitting. After training using the complete 800-sample cohort, the final model was applied to the independent external cohort. During training, the mean training loss was computed for each epoch, and classification accuracy was recorded for the complete training cohort. As shown in Figure 6c, the training loss decreased rapidly during the initial epochs and subsequently stabilized, whereas the training accuracy increased and reached a relatively stable plateau, indicating convergence of the model-training process.

t-distributed stochastic neighbor embedding (t-SNE), a dimensionality reduction technique, was applied to visualize the learned feature representations of the 160 samples in the independent external cohort. Each point on the plot represents one external-test sample projected from the high-dimensional feature space into two dimensions. The visualization shows state-dependent feature distributions, with partial overlap among samples from different fatigue states. The t-SNE dimensions are unitless coordinates and are presented as a qualitative representation of similarity in the learned feature space. These results suggest that the extracted features contain information relevant to discrimination among the four fatigue states in previously unseen participants. To evaluate model performance, one-vs-rest receiver operating characteristic (ROC) analysis was conducted using the prediction probabilities obtained from the independent external cohort (Figure S37). The model achieved AUC values of 0.98, 0.96, 0.95, and 0.99 for the relaxed, mild, moderate, and severe fatigue states, respectively. The final classification results are summarized in the confusion matrix in Figure 6e, showing an overall recognition accuracy of 83.1% (133 correctly classified samples out of 160; 95% confidence interval: 76.6%–88.1%). The class-specific recognition rates for the relaxed, mild, moderate, and severe fatigue states were 87.5%, 77.5%, 75.0%, and 92.5%, respectively. The lower recognition rates for the mild and moderate states indicate that the intermediate fatigue states were comparatively more difficult to distinguish. These results indicate that the multichannel array device, coupled with machine learning, holds potential for classification of muscle fatigue states in participants who were not included in model training. An additional validation experiment using the Borg CR10 rating of perceived exertion scale showed a strong positive correlation between the number of fatigued channels and Borg CR10 scores (Spearman's $\rho = 0.959$, 95% CI [0.951, 0.968], $p < 0.001$; 40 participants and 160 trials; Figure S38a). Borg CR10 scores also increased progressively across the four sEMG-defined fatigue states (Figure S38b and Tables S5 and S6), providing additional physiological support for the classification framework.

3 | Discussion

We developed a mechanically compliant, multichannel surface electromyography (sEMG) platform that enables stable, high-fidelity signal acquisition during dynamic motion. This was achieved by overcoming the electromechanical instability and motion-induced signal degradation common in conventional sEMG systems through the integration of a bacterial cellulose (BC)-reinforced heterogeneous eutectogel electrode with a laser-cut, hollow-patterned flexible printed circuit (FPC) substrate. The eutectogel architecture dissipates mechanical stress and maintains ionic conductivity under repeated deformation, while the patterned FPC structure redistributes strain and minimizes inter-channel crosstalk. Together, these features support multichannel sEMG acquisition with reduced motion artifacts.

The platform demonstrates exceptional mechanical and electrical robustness, maintaining negligible resistance drift over 100 000 bending cycles and stable impedance across a broad frequency range. These properties enable spatially resolved tracking of muscle activities and extraction of fatigue-related features. Based on the multichannel signals, a deep learning model achieved an accuracy of 83.1% when evaluated on 160 samples from an independent cohort of 40 previously unseen participants, demonstrating the feasibility of fatigue-state classification using this platform across participants who were not included in model training. The comparatively higher recognition rates for the relaxed and severe states and the lower recognition rates for the mild and moderate states suggest that the endpoints of the fatigue continuum were more distinguishable than the intermediate states.

The platform demonstrates mechanical and electrical stability over 100 000 bending cycles and across a broad frequency range, enabling spatially resolved tracking of muscle activities and

16163028, 0, Downloaded from https://advanced.onlinelibrary.wiley.com/doi/10.1002/adfm.78406 by Beihang University (Buaa), Wiley Online Library on [23/09/2026]. See the Terms and Conditions (https://onlinelibrary.wiley.com/terms-and-conditions) on Wiley Online Library for rules of use; OA articles are governed by the applicable Creative Commons License

extraction of fatigue-related features. Based on the multichannel signals, a deep learning model achieved an accuracy of 83.1% when evaluated using 160 samples from an independent cohort of 40 previously unseen participants, demonstrating the feasibility of fatigue-state classification in participants who were not included in model training. The comparatively higher recognition rates for the relaxed and severe states indicate that these endpoint states were more distinguishable than the intermediate states. Borg CR10 scores also increased progressively across the four sEMG-defined fatigue states, providing additional support for the physiological relevance of the classification framework. MDF/MNF analysis and the CNN–BiLSTM provide complementary functions for interpretable channel-level assessment and automated multichannel state recognition, respectively, although further validation using objective physiological measures is warranted.

Despite its promising performance, several areas offer room for further enhancement: (i) Under extreme or highly non-uniform deformation, gradual signal degradation may occur, suggesting the need to incorporate intrinsically stretchable substrates to improve mechanical compliance. (ii) Increasing array density and spatial coverage could enable more comprehensive mapping of muscle coordination and complex biomechanical patterns. (iii) As the current eutectogel interface is inherently non-adhesive, external fixation is required; integrating bioadhesive materials or skin-compatible anchoring strategies could improve wearability and long-term stability during high-mobility activities.

In summary, this work presents a multichannel electrophysiological platform capable of stable signal acquisition under motion. By combining soft-material design with multichannel signal analysis, the system provides an approach for neuromuscular monitoring with potential applications in exercise-related scenarios.

4 | Materials and Methods

A detailed Experimental Section can be found in the Supporting Information. All experiments involving human participants were carried out upon approval from the Beijing Forestry University Committee on the Use of Humans as Experimental Subjects (202400102).

Acknowledgements

This work is financially supported by 5·5 Engineering Research & Innovation Team Project of Beijing Forestry University (BLRC2023B01), Beijing Natural Science Foundation (L252200), National Natural Science Foundation of China (52125205, 52532005, 52250398, and 22672013), National Key Research and Development (R&D) Program from Ministry of Science and Technology of China (2024YFB3814100). In addition, the authors would like to appreciate the assistance from the Innovation Platform for High-Value Utilization of Forest Resources, Beijing Forestry University. The authors also thank Xuzhou B&C Chemical Co. Ltd for providing the photoresist (HTA116, HTA112, B&C Chemicals) used in our work.

Conflicts of Interest

The authors declare no conflicts of interest.

Data Availability Statement

The data that support the findings of this study are available in the supplementary material of this article.

References

1. C. Xu, Y. Song, J. R. Sempionatto, et al., "A Physicochemical-Sensing Electronic Skin for Stress Response Monitoring," *Nature Electronics* 7 (2024): 168–179, https://doi.org/10.1038/s41928-023-01116-6.

2. B. Kang, N. Zavanelli, G. N. Sue, S. Chen, M. K. Kim, and Y. Lee, "A Flexible Skin-Mounted Haptic Interface for Multimodal Cutaneous Feedback," *Nature Electronics* 8 (2025): 818–830, https://doi.org/10.1038/s41928-025-01443-w.

3. Y. Zhan, J. Poisson, X. Meng, et al., "Electrospun Lignin/ZnO Nanofibrous Membranes for Self-Powered Ultrasensitive Flexible Airflow Sensor and Wearable Device," *Advanced Materials* 37 (2025): 2502211, https://doi.org/10.1002/adma.202502211.

4. N. A. Dimitrova and G. V. Dimitrov, "Interpretation of EMG Changes With Fatigue: Facts, Pitfalls, and Fallacies," *Journal of Electromyography and Kinesiology* 13 (2003): 13–36, https://doi.org/10.1016/S1050-6411(02)00083-4.

5. J. L. Taylor, M. Amann, J. Duchateau, R. Meeusen, and C. L. Rice, "Neural Contributions to Muscle Fatigue: From the Brain to the Muscle and Back Again," *Medicine and Science in Sports and Exercise* 48 (2016): 2294.

6. N. K. Vollestad, "Measurement of Human Muscle Fatigue," *Journal of Neuroscience Methods* 74 (1997): 219–227, https://doi.org/10.1016/S0165-0270(97)02251-6.

7. D. Abdessemed, P. Duché, C. Hautier, G. Poumarat, and M. Bedu, "Effect of Recovery Duration on Muscular Power and Blood Lactate During the Bench Press Exercise," *International Journal of Sports Medicine* 20 (1999): 368–373.

8. S. Yang, J. Cheng, J. Shang, et al., "Stretchable Surface Electromyography Electrode Array Patch for Tendon Location and Muscle Injury Prevention," *Nature Communications* 14 (2023): 6494, https://doi.org/10.1038/s41467-023-42149-x.

9. K. van Oosterhout, S. van Diemen, M. Timmermans, M. Fattori, M. Sartori, and E. Cantatore, "Flexible Circuits for Bionic Limbs: A High Impedance Multiplexing Front-End for Myoelectric Control," *npj Flex Electron* 9 (2025): 117.

10. I. B. Abdallah, Y. Bouteraa, and A. Alotaibi, "A Hybrid EMG–EEG Interface for Robust Intention Detection and Fatigue-Adaptive Control of an Elbow Rehabilitation Robot," *Scientific Reports* 15 (2025): 40895, https://doi.org/10.1038/s41598-025-24831-w.

11. L. Pan, P. Cai, L. Mei, et al., "A Compliant Ionic Adhesive Electrode With Ultralow Bioelectronic Impedance," *Advanced Materials* 32 (2020): 2003723, https://doi.org/10.1002/adma.202003723.

12. C. C. D. S. Novais, A. R. O. D. R. Santana, A. R. Moura da Paz, A. T. L. Carnaúba, K. C. L. Andrade, and P. L. Menezes, "The Impact of Using Electromyographic Biofeedback on Pelvic Floor Rehabilitation in Men With Post-Prostatectomy Urinary Incontinence: A Meta-Analysis," *Clinics* 80 (2025): 100687, https://doi.org/10.1016/j.clinsp.2025.100687.

13. K. K. Kim, T. J. Zaluska, S. Skov, et al., "A Simplified Wearable Device Powered by a Generative EMG Network for Hand-Gesture Recognition and Gait Prediction," *Nature Sensors* 1 (2026): 27–38, https://doi.org/10.1038/s44460-025-00002-2.

14. A. Greco, G. Valenza, A. Bicchi, M. Bianchi, and E. P. Scilingo, "Assessment of Muscle Fatigue During Isometric Contraction Using Autonomic Nervous System Correlates," *Biomedical Signal Processing and Control* 51 (2019): 42–49, https://doi.org/10.1016/j.bspc.2019.02.007.

15. Y. Zhao, W. Gao, K. Dai, et al., "Bioinspired Multifunctional Photonic-Electronic Smart Skin for Ultrasensitive Health Monitoring, for Visual and Self-Powered Sensing," *Advanced Materials* 33 (2021): 2102332, https://doi.org/10.1002/adma.202102332.

16163028, 0, Downloaded from https://advanced.onlinelibrary.wiley.com/doi/10.1002/adfm.78406 by Beihang University (Buaa), Wiley Online Library on [23/09/2026]. See the Terms and Conditions (https://onlinelibrary.wiley.com/terms-and-conditions) on Wiley Online Library for rules of use; OA articles are governed by the applicable Creative Commons License

16. W. Heng, S. Solomon, and W. Gao, "Flexible Electronics and Devices as Human–Machine Interfaces for Medical Robotics," *Advanced Materials* 34 (2022): 2107902, https://doi.org/10.1002/adma.202107902.

17. T.-G. La and L. H. Le, "Flexible and Wearable Ultrasound Device for Medical Applications: A Review on Materials, Structural Designs, and Current Challenges," *Advanced Materials Technologies* 7 (2022): 2100798, https://doi.org/10.1002/admt.202100798.

18. S. Gong, Y. Lu, J. Yin, A. Levin, and W. Cheng, "Materials-Driven Soft Wearable Bioelectronics for Connected Healthcare," *Chemical Reviews* 124 (2024): 455–553, https://doi.org/10.1021/acs.chemrev.3c00502.

19. Q. Han, X. Gao, C. Zhang, et al., "Acid-Induced in Situ Phase Separation and Percolation for Constructing Bi-Continuous Phase Hydrogel Electrodes With Motion-Insensitive Property," *Advanced Materials* 37 (2025): 2415445, https://doi.org/10.1002/adma.202415445.

20. C. M. Reis, M. R. Carneiro, C. Majidi, and M. Tavakoli, "Gallium-Based Liquid–Solid Biphasic Conductors for Soft Electronics," *Advanced Functional Materials* 33 (2023): 2306453, https://doi.org/10.1002/adfm.202306453.

21. X. Li, E. Rytkin, Q. Zhao, et al., "High-Resolution Liquid Metal–Based Stretchable Electronics Enabled by Colloidal Self-Assembly and Microtransfer Printing," *Science Advances* 11 (2025): adw3044.

22. M. D. Dickey, "Stretchable and Soft Electronics using Liquid Metals," *Advanced Materials* 29 (2017): 1606425, https://doi.org/10.1002/adma.201606425.

23. A. Jannat, M. M. M. Talukder, Z. Li, and J. Z. Ou, "Recent Advances in Flexible and Wearable Gas Sensors Harnessing the Potential of 2D Materials," *Small Science* 5 (2025): 250002.

24. Y. Shi, J. Zhang, A. M. Bruck, et al., "A Tunable 3D Nanostructured Conductive Gel Framework Electrode for High-Performance Lithium Ion Batteries," *Advanced Materials* 29 (2017): 1603922, https://doi.org/10.1002/adma.201603922.

25. X. Gao, Y. Bao, Z. Chen, et al., "Bioelectronic Applications of Intrinsically Conductive Polymers," *Advanced Electronic Materials* 9 (2023): 2300082, https://doi.org/10.1002/aelm.202300082.

26. D. Yang, G. Tian, J. Chen, et al., "Microscale Confined Adhesion Strategy for Liquid Metal-Based Highly Stretchable Bioelectrode Arrays," *Advanced Functional Materials* 36 (2025): 13875.

27. A. R. Hassan, Z. Zhao, J. J. Ferrero, et al., "Translational Organic Neural Interface Devices at Single Neuron Resolution," *Advanced Science* 9 (2022): 2202306, https://doi.org/10.1002/advs.202202306.

28. J. Matthews, J. Kim, and W. Yeo, "Advances in Biosignal Sensing and Signal Processing Methods With Wearable Devices," *Analysis & Sensing* 3 (2023): 202200062.

29. J. Yin, S. Wang, T. Tat, and J. Chen, "Motion Artefact Management for Soft Bioelectronics," *Nature Reviews Bioengineering* 2 (2024): 541–558, https://doi.org/10.1038/s44222-024-00175-4.

30. T. H. Kim, C. Bao, Z. Chen, and W. S. Kim, "3D Printed Leech-Inspired Origami Dry Electrodes for Electrophysiology Sensing Robots," *npj Flexible Electronics* 6 (2022): 5, https://doi.org/10.1038/s41528-022-00139-x.

31. S. K. Ameri, M. Kim, I. A. Kuang, et al., "Imperceptible Electrooculography Graphene Sensor System for Human–Robot Interface," *npj 2D Materials and Applications* 2 (2018): 19, https://doi.org/10.1038/s41699-018-0064-4.

32. S. Han, Y. Yue, M. Razbin, et al., "Geometry-Engineered Hourglass-Shaped Cracks Enable Wide-Linearity Wearable Strain Sensors," *Materials Horizons* 13 (2026): 5550–5561.

33. J. Park, J. Jeong, M. Kang, et al., "Imperceptive and Reusable Dermal Surface EMG for Lower Extremity Neuro-Prosthetic Control and Clinical Assessment," *npj Flexible Electronics* 7 (2023): 49, https://doi.org/10.1038/s41528-023-00282-z.

34. L. Xu, S. R. Gutbrod, A. P. Bonifas, et al., "3D Multifunctional Integumentary Membranes for Spatiotemporal Cardiac Measurements and Stimulation Across the Entire Epicardium," *Nature Communications* 5 (2014): 3329, https://doi.org/10.1038/ncomms4329.

35. J. C. Yang, S. Lee, B. S. Ma, et al., "Geometrically Engineered Rigid Island Array for Stretchable Electronics Capable of Withstanding Various Deformation Modes," *Science Advances* 8 (2022): abn3863, https://doi.org/10.1126/sciadv.abn3863.

36. Y. Li, X. Zhang, Y. Xie, et al., "Achieving Tissue-Level Softness on Stretchable Electronics Through a Generalizable Soft Interlayer Design," *Nature Communications* 14 (2023): 4488, https://doi.org/10.1038/s41467-023-40191-3.

37. H. C. Ates, P. Q. Nguyen, L. Gonzalez-Macia, et al., "End-to-End Design of Wearable Sensors," *Nature Reviews Materials* 7 (2022): 887–907, https://doi.org/10.1038/s41578-022-00460-x.

38. M. R. Carneiro, M. Tavakoli, and C. Majidi, "Soft Skin-interfacing Electrodes for Wearable Bioelectronics," *Matter* 8 (2025): 102409, https://doi.org/10.1016/j.matt.2025.102409.

39. W. Yang, S. Liu, Z. Wang, et al., "Bioinspired Composite Fiber Aerogel Pressure Sensor for Machine-Learning-Assisted Human Activity and Gesture Recognition," *Nano Energy* 127 (2024): 109799, https://doi.org/10.1016/j.nanoen.2024.109799.

40. B. Lu, S. Xie, L. Zhang, et al., "Pure PEDOT:PSS Hydrogels," *Nature Communications* 10 (2019): 1043, https://doi.org/10.1038/s41467-019-09003-5.

41. T. Li, X. Zhang, Y. Zhou, et al., "Robust Skin-Integrated Conductive Biogel for High-Fidelity Detection Under Mechanical Stress," *Nature Communications* 16 (2025): 88, https://doi.org/10.1038/s41467-024-55417-1.

42. M. Saadi, H. Liu, F. Li, et al., "Flow-Induced 2D Nanomaterials Intercalated Aligned Bacterial Cellulose," *Nature Communications* 16 (2025): 5825, https://doi.org/10.1038/s41467-025-60242-1.

43. X. Lu, W. Wang, X. Zhang, et al., "Triboelectric Sensor Gloves for Real-Time Behavior Identification and Takeover Time Adjustment in Conditionally Automated Vehicles," *Nature Communications* 16 (2025): 1080, https://doi.org/10.1038/s41467-025-56169-2.

Supporting Information

Additional supporting information can be found online in the Supporting Information section.

Supporting File 1: adfm78406-sup-0001-SuppMat.docx.

Supporting File 2: adfm78406-sup-0002-MovieS1.mp4.

Supporting File 3: adfm78406-sup-0003-MovieS2.mp4.

Supporting File 4: adfm78406-sup-0004-MovieS3.mp4.

16163028, 0, Downloaded from https://advanced.onlinelibrary.wiley.com/doi/10.1002/adfm.78406 by Beihang University (Buaa), Wiley Online Library on [23/09/2026]. See the Terms and Conditions (https://onlinelibrary.wiley.com/terms-and-conditions) on Wiley Online Library for rules of use; OA articles are governed by the applicable Creative Commons License